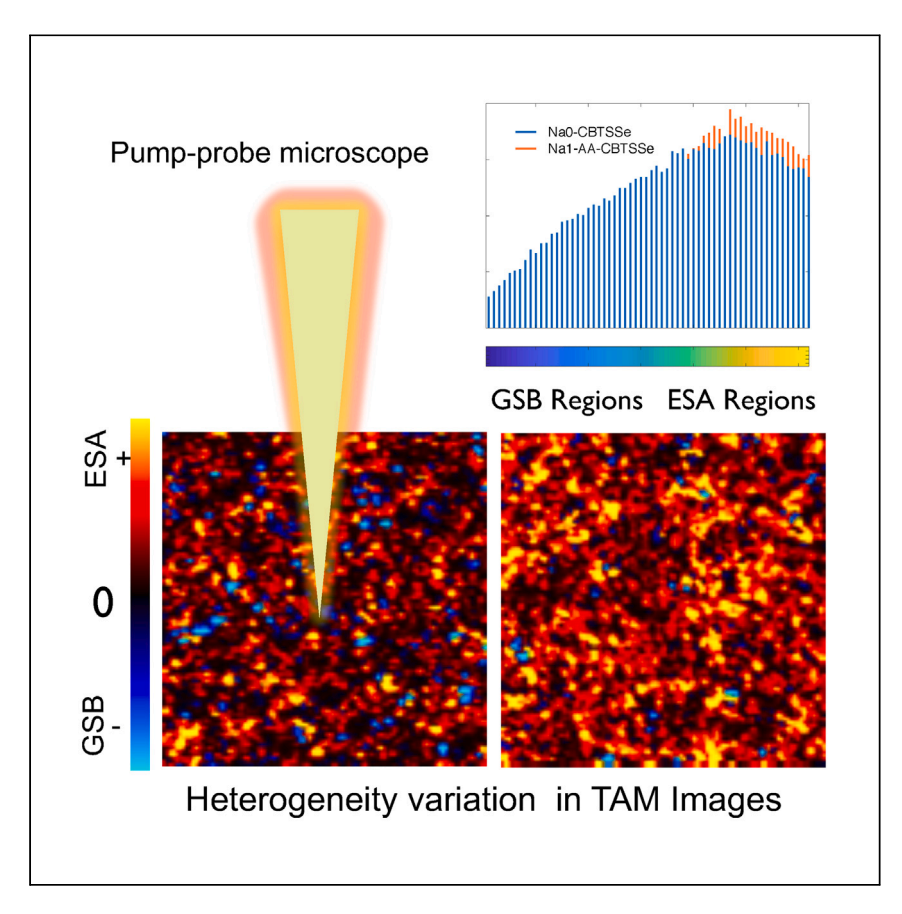


Article

Ultrafast microscopy and image segmentation of spatially heterogeneous excited state and trap passivation in Cu₂BaSnSSe₃



Ghadiri et al. integrate two-color pump-probe diffuse reflectance microscopy to visualize the photoexcited pattern in CBTSSe films. The statistical and principal-component analyses quantify the heterogeneity of the photoexcited patterns. The heterogeneity of the excited state pattern is affected by the solution processing of the films; namely, sodium doping and air annealing.

Hannah Luebbering, Ashkan Shafiee, Betul Teymur, Yongshin Kim, David B. Mitzi, Elham Ghadiri

Ghadire@wfu.edu

Highlights

Transient absorption microscopy to visualize the photoexcited pattern in materials

Controlling the heterogeneity of TAM images by solution processing of the films

Statistical analysis and principalcomponent analysis for quantified image analysis

Stable charge carriers in solution-processed CBTSSe films

Luebbering et al., Cell Reports Physical Science 4, 101601

October 18, 2023 © 2023 The Authors. https://doi.org/10.1016/j.xcrp.2023.101601





Article

Ultrafast microscopy and image segmentation of spatially heterogeneous excited state and trap passivation in Cu₂BaSnSSe₃

Hannah Luebbering, ^{1,2} Ashkan Shafiee, ^{2,3} Betul Teymur, ⁵ Yongshin Kim, ⁵ David B. Mitzi, ^{4,5} and Elham Ghadiri ^{1,2,3,6,*}

SUMMARY

Earth-abundant Cu₂BaSnS_{4-x}Se_x (CBTSSe) represents a recent alternative for Cu₂ZnSn(S,Se)₄ for solar energy conversion with a lower level of disorder and band tailing. We report the heterogeneous excited-state and trap-state pattern in different solution-processed CBTSSe films using ultrafast two-color pump-probe diffuse reflectance microscopic imaging. The spectroscopy/microscopy method can visualize and correlate the microscopic compositional and electronic variations (i.e., trap states) in real space with time-resolved photophysics. Heterogeneity patterns in TAM images show that some grains exhibit a positive excited-state absorption (ESA) signal, while others show negative ground-state bleaching (GSB). Our results visualize that film processing, such as air annealing and Na addition, has a clear influence on the heterogeneity of the excitedstate pattern. Importantly, we report stable charge carrier over 100 ps. We applied the image principal component and histogram for quantitative analysis of TAM images to deconvolute and visualize the contribution and fingerprints of minority free carriers and sub-band-gap trapped carriers.

INTRODUCTION

Multinary chalcogenide semiconductors (e.g., Cu(In,Ga)(S,Se)₂ [CIGSSe] and Cu₂ZnSn(S,Se)₄ [CZTSSe]) have been adopted as thin-film solar absorbers for electricity production in photovoltaic (PV) and photoelectrochemical (PEC) devices. However, scarcity of In in CIGSSe and poor defect properties of CZTSSe limit their long-term and large-scale application. The poor defect properties of CZTSSe that limit power conversion efficiency (PCE) improvement stem partially from the chemical/electronic similarities of Cu/Zn and their tendency to replace each other within the CZTSSe lattice.² To circumvent these obstacles, an emerging family of materials that replace Zn in CZTSSe with larger ions, such as Ba or Sr, has been proposed.³⁻⁶ Materials in this family are expected to be disorder resistant (i.e., to have lower densities of intrinsic defects that can adversely impact optoelectronic properties) because of the ionic size and coordination differences among the component metals. For example, a material of this family, earth-abundant Cu₂BaSnS_xSe_{4-x} (CBTSSe), has been shown recently to have a lower level of disorder, with initial PV and PEC devices exceeding 5% PCE without detailed device optimization. 5,6 These initial results are based on CBTSSe films deposited by vacuum-based approaches (i.e., sputtering). Given the expected dependence of defect chemistry on film growth conditions coupled with prospective processing benefits, examination of solution processing for film deposition is also of interest; e.g.,



¹Department of Chemistry, Wake Forest University, Winston-Salem, NC 27109, USA

²Center for Functional Materials, Wake Forest University, Winston-Salem, NC 27109, USA

³Wake Forest School of Medicine, Wake Forest University, Winston-Salem, NC 27157, USA

⁴Department of Chemistry, Duke University, Durham, NC 27708, USA

⁵Department of Mechanical Engineering and Materials Science, Duke University, Durham, NC 27708, USA

⁶Lead contact

^{*}Correspondence: Ghadire@wfu.edu https://doi.org/10.1016/j.xcrp.2023.101601





solution-processed CBTSSe thin films used for PEC applications have been demonstrated using low-toxicity dimethyl sulfoxide as a solvent.⁸ Recently, solution-processed PV devices have also been demonstrated, with PCE exceeding 6%.⁹

A detailed understanding of photophysical processes, such as charge carrier photogeneration, recombination dynamics, the role of various defects, and their influence on the carrier lifetime in these recently developed solution-processed CBTSSe films, is essential. In general, a spectroscopic/optoelectronic characterization approach that can identify such processes in solar cell devices or visualize and correlate their microscopic origins in real space with the time-resolved photophysics is indispensable. Pump-probe techniques, including transient absorption spectroscopy (TAS), provide insights into ultrafast photophysical processes in materials (namely, excited-state characteristics, the spectral signature of photocarrier absorption, charge separation, trapping, and recombination dynamics) within a femtosecond to nanosecond time frame. 10-12 Despite the great potential of conventional transmission-based TAS, the main limitation of this technique is that the samples must be optically transparent. Therefore, conventional transmissionbased TAS is not sufficiently versatile for the study of many opaque materials, highly light-absorbing samples, or thin films deposited on conductive metallic substrates. We have previously demonstrated ultrafast time-resolved pump-probe diffuse reflectance (DR) spectroscopy (DR-TAS) with a sub-200-fs time resolution. 13 The technique has enabled study of ultrafast charge carrier dynamics in functional opaque dye-sensitized solar cells (DSCs), highly light-absorbing/scattering materials, 13-16 and vacuum-deposited CBTSSe films on Mo substrates. 5 Notably, the optical absorption coefficients of the CBTSSe chalcogenides are exceptionally high. The absorption coefficient for CBTS is about 10⁴ cm⁻¹ for the range of photon energies above the band gap. 17 Therefore, even thin films of this material look dark and relatively opaque gray with no specular reflection. This observation suggests that studies of the photophysical dynamics involved should be performed more precisely using DR-TAS. We also integrated DR-TAS with pump-probe confocal microscopy (fs-DR-TAM) and showed that the technique allows localization of charge carrier kinetics in small grains. We demonstrated that the technique provides useful insights into the dynamic behavior of charge carriers within fewhundred-nanometer-scale grains of vacuum-deposited CBTSSe layers. For vacuum-deposited CBTSSe thin films, we observed that early recombination of the majority of charge carriers happens in sub-20 ps. These observations suggest that the charge carrier processes should be improved for these films to further enhance device performance.⁵

It is important to clarify and note the importance of recent methodological advancements for establishing non-invasive methods for thermal or artifact-free spectroscopy methods. Traditionally, time-resolved DR measurements are performed using a laser flash photolysis method, which applies low repetition rates and dramatically high excitation pulse energies. DR spectroscopy in a microsecond time frame was first reported by Kessler and Wilkinson 18 in 1981 using an optical lens to collect 3%-4% of the diffuse reflected light of powders in a laser flash photolysis scheme. Dramatically high excitation energies of 20 mJ/pulse (64 mJ/cm²) caused interfering photothermal effects. 19 For nanosecond DR-TAS, we previously used ellipsoidal mirrors intercepting $\sim\!20\%$ of the total reflection at all angles, $0^\circ\!-\!90^\circ$, of opaque DSC samples at much lower excitation pulse energies of 50–200 μ J/cm². 15 By increasing the solid angle of DR light collection and applying laser pulses (with a low energy of 100 nJ) that provide a fluence on the order of 100 μ J/cm², we resolved DR spectroscopy at sub-200-fs time resolution and verified the agreement of transmission and

Article



DR-based measurements and photostability of the chromophores after several measurements.¹³ Two-color microscopy using megahertz repetition with lock-in detection allows a high signal-to-noise ratio at low pulse energies, which eliminates thermal effects as a non-invasive method. Using two-color TAM, the spatial variation in electron-hole recombination in ZnO rods was reported.²⁰ By scanning probe versus pump, this method was incorporated to study charge separation, transport, and recombination in nanowires^{21–24} and perovskites²⁵ and (using non-linear contrast) for biomedical imaging²⁶ and artwork.²⁷ The ultrafast microscopy in DR mode, the same as in transmission modes, applies much less pulse energy (on the order of picojoules) and energy fluences typically of 0.5-1 mJ/cm² as a non-invasive method for photochemical analysis of samples.⁵ Time-resolved photoemission electron microscopy (TR-PEEM) has been reported for photodynamic study.²⁸ However, in TR-PEEM, the high photon flux of the applied laser pulses needed for the photoemission process results in strong charging effects in the sample that disallow study of higher-resistivity samples, such as semiconductors. Despite the high spatial resolution, the low penetration depth of electrons is another challenge in TR-PEEM, and, in general, stricter sample and instrumentation requirements, such as an ultrahigh vacuum, make them less effective to measure real functional samples and devices made of multilayers of materials.

The important aspects of the current manuscript are (1) emerging materials development with advanced photophysical characteristics suitable for energy conversion applications, (2) integration of advanced ultrafast microscopy methods for photophysical analysis of materials at few-hundred-nanometer spatial resolution, and (3) a first-time report of microscopic visualization and quantified analysis of electronic trap states and their passivation for relating the photochemistry to electronic variations. The current manuscript is a first-time report of the photophysical analysis of CBTSSe materials prepared by a solution method using pump-probe DR microscopy. In this study, we address the issue of the very short charge carrier lifetime observed in CBTSSe thin films prepared by vacuum deposition. Remarkably, we show that charge carriers are stable in solution-based CBTSSe films for hundreds of picoseconds. We perform DR-TAM microscopy to spatially localize the excitedstate pattern in solution-processed films. We also study the effect of Na addition and air annealing treatment of the films on the heterogeneity of the ultrafast pump-probe TAS images. We observe that solution processing and film post-deposition treatment impact the ultrafast excited-state absorption (ESA) pattern in DR-TAM images. Na addition and air annealing enhance the homogeneity of the ESA pattern. The spatial and spectral heterogeneity can be due to the existence of shallow traps, which cause energy variations and band tailing.

RESULTS AND DISCUSSION

Structural and elemental analysis of CBTSSe samples

For spectroscopic analysis, we used solution-processed CBTSSe films prepared with different Na mole concentrations (0% and 1%) on Mo/soda lime glass (experimental procedures). The phase and chemical composition of the films were characterized by X-ray diffraction (XRD) and inductively coupled plasma mass spectrometry (ICP-MS) (Table S1) analyses. The depth profile of the elemental components was defined by time-of-flight secondary ion mass spectrometry (TOF-SIMS) (Figure S1). A detailed discussion of Na content analysis using ICP-MS and TOF-SIMS is provide in Note S1. The notation 0% Na does not represent the absence of Na in the film because there can be diffusion of Na from the glass itself; rather, it represents no excess amount of Na added during film precursor solution preparation. XRD patterns of



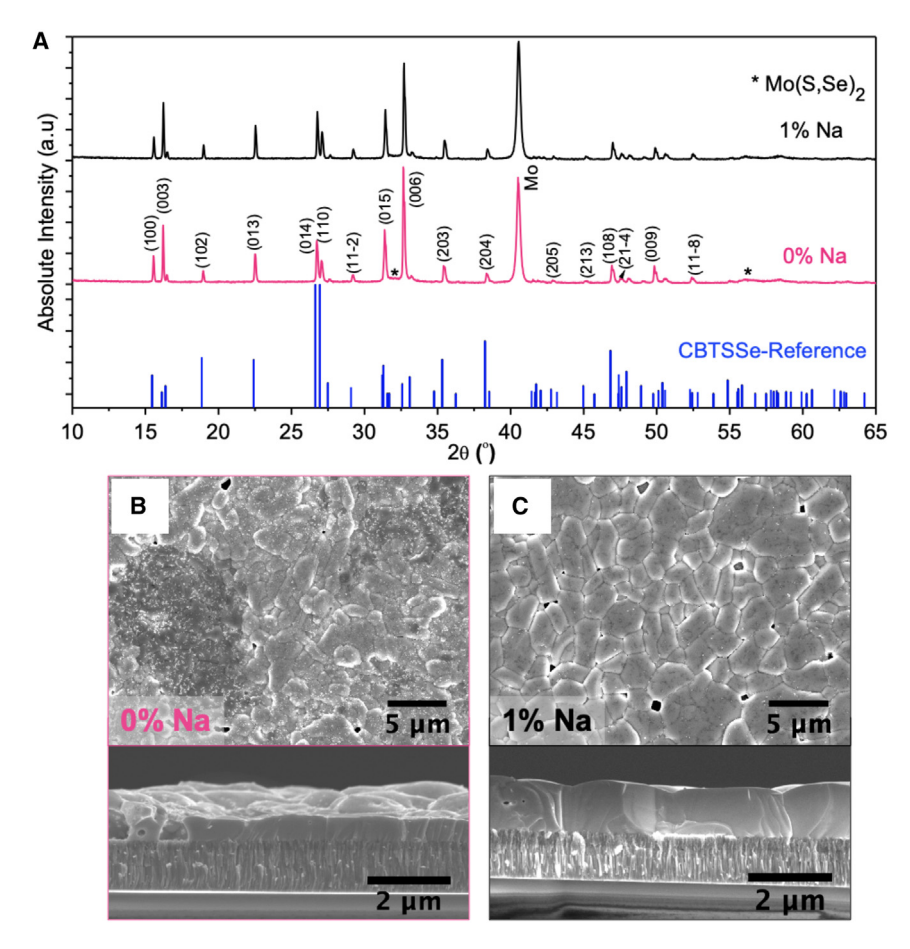


Figure 1. Crystalline structure and morphological analysis of the CBTSSe films (A) XRD profiles of CBTSSe films for externally introduced Na atomic ratio to all other metal ions (Na/[Cu + Ba + Sn]) = 0, 0.01. Miller indices for the major XRD peaks are determined by fitting with the reference XRD (blue stick pattern) for trigonal structure $Cu_2BaSnS_{4-x}Se_x$ ($P3_1$) (x=3). (B and C) Top-view and cross-section SEM images of the films with (B) 0%-Na additive and (C) 1%-Na additive.

CBTSSe films with 0% and 1% Na mole concentrations (Figure 1A) show a single $P3_1$ space group phase of CBTSSe with no impurity phases detected. The ICP-MS results (Table S1) indicate that current films exhibit a nominally stoichiometric to slightly Barich metal composition; for example, with [Cu]/([Ba]+[Sn]) = 0.99 \pm 0.05 and [Ba]/[Sn] = 1.05 \pm 0.05 for the 1% Na film. The %[Na]/([Ba]+[Sn]+ [Cu]) values are 1.30% for the 1%-Na sample and 0.71% for the 0%-Na sample.

The top-view scanning electron microscopy (SEM) images of 1% -Na CBTSSe and 0%-Na CBTSSe films (Figures 1B and 1C) confirm that Na addition improves grain growth. After selenization, both films show large grains, with a greater number of larger grains for the films with Na additive. The lengths of a total of nine lines on the SEM image were divided by the number of grains that intersected the lines to calculate the average grain size. 1%-Na CBTSSe films have an average grain size of 2.2 μ m, whereas 0%-Na CBTSSe films show an average of 1.3 μ m. The average grain size enlargement and enhanced uniformity with Na additive decreases the density of grain boundaries that can potentially serve as recombination centers for charge carriers. As indicated in the cross-section image of the 0%-Na film (Figure 1B),



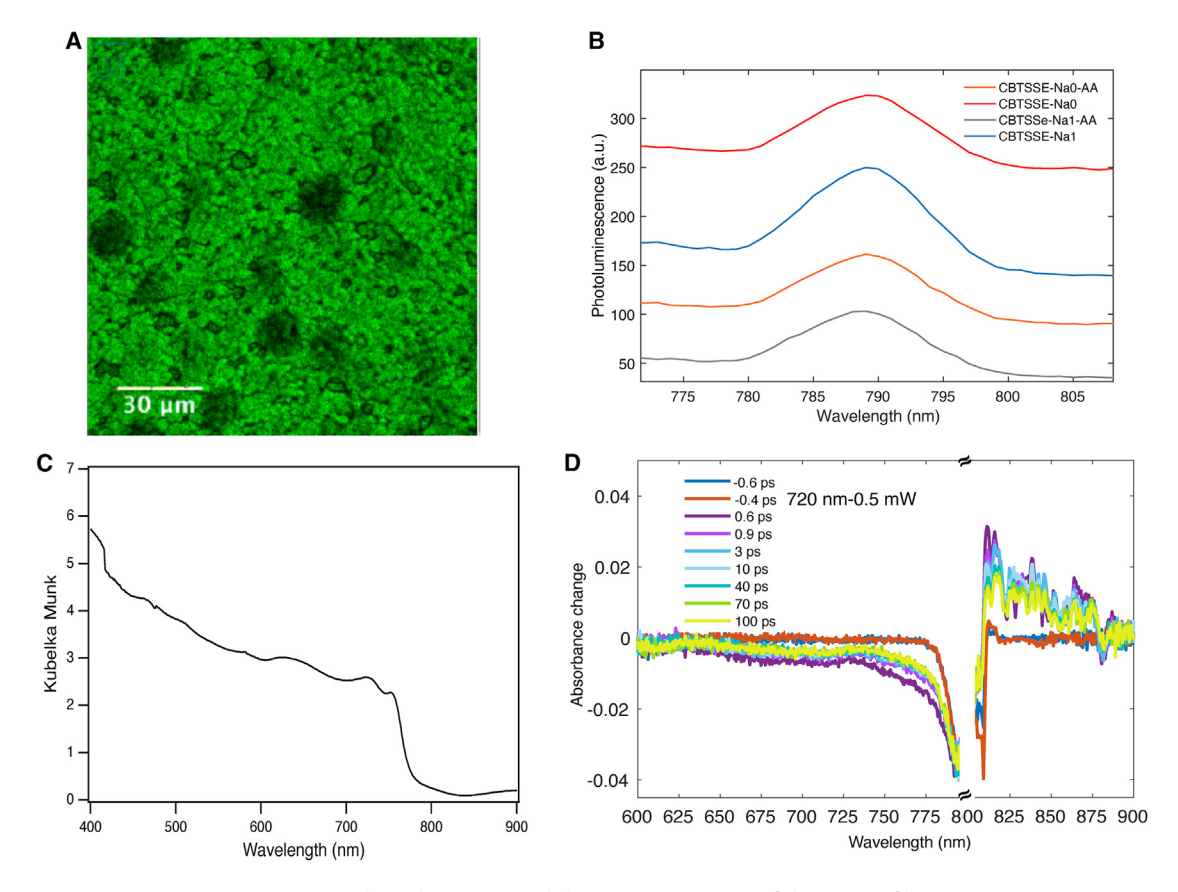


Figure 2. PL microscopic image, PL spectra, and steady-state optical absorptance spectrum of the CBTSSe films

(A) The typical confocal PL images resolve grains of \sim 5 μm and show uniform PL across the entire large scanned area. The darker areas correspond to surface morphology that reduces the collection of PL. $\lambda_{\rm exc}=633$ nm.

(B) The PL spectrum for the four solution-processed CBTSSe samples, including air annealing (AA) and 1%-Na addition. All samples show a PL peak at 790 nm. $\lambda_{\text{exc}} = 633 \text{ nm}$.

(C) Kubelka-Munk spectrum of a solution-processed CBTSSe film.

(D) Broadband DR-TAS of the CBTSSe film. The negative peak centered around 780 nm corresponds to the GSB. The positive feature above 807 nm belongs to ESA, which reflects photoabsorption by photogenerated minority carriers. The excitation is at 720 nm, and the broadband spectrum is measured from 600 nm. The wavelength range of 795–806 nm is eliminated because of spectral overlap with the fundamental laser wavelength.

darker spots appearing on the top-view image represent CBTSSe grains with different thicknesses (0.8–1.1 μm). Formation of larger columnar grains with fewer grain boundaries is observed in 1% -Na CBTSSe films (Figure 1C), with a more uniform thickness of approximately 1 μm all over the surface. Therefore, one role of Na addition (in the form of NaCl) appears to be improvement of film morphology and providing a pathway to improve grain size.

Atomic force microscopy (AFM) analysis (Figure S2; Note S2) is also used to discuss the film morphology of the CBTSSe samples and the effect of Na content on it, and the results show, in the case of the 1%-Na film, that the grains are slightly bigger; however, the 0%-Na film has reduced surface roughness (Rq).

A typical photoluminescence (PL) image of a CBTSSe film (Figure 2A) exhibits nominally homogeneous PL across the large scan area. The PL spectrum for all four samples (with or without air annealing, with or without added Na) shows a PL peak at 790 nm (Figure 2B), which is not changed upon film processing. NIR-PL images of different films (CBTSSe-Na0, CBTSSe-Na1, and CBTSSe-air annealing



[AA]-Na1) are provided in Figure S3. Because of the weak PL of CBTSSe, it is challenging to use PL for extensive quantitative analysis. Therefore, we used this technique to look at the homogeneity and structure of the films and the spectral location of the PL peaks. The Kubelka-Munk spectrum of the CBTSSe film (Figure 2C), is characterized by a relatively sharp band edge at 770 nm with no residual absorption at 820 nm. The PL peak is spectrally located close to the absorption band edge. The broadening of the CBTSSe film PL is remarkably smaller than that reported for analogous CZTSSe materials (~190 nm full-width half-maximum [FWHM], 180 meV).^{2,17} These observations indicate that near-band-edge states in CBTSSe are less prevalent compared with CZTSSe films. Low-temperature and fluence-dependent PL studies on samples prepared similarly as in the current work have been conducted to quantitatively investigate the nature and energetics of defects in this material and compare them with DFT studies.²⁹ Briefly, at low temperatures (15-100 K), major defect PL was observed at 1.5 eV, for which the PL intensity varies with excitation power and with a slight spectral shift depending on temperature.²⁹ The external PL quantum yield (radiative recombination) at room temperature is low for CBTSSe material (\sim 4 x 10⁻¹¹ at 1-sun-equivalent excitation), and high excitation energies are required.²⁹ Therefore, while PL measurements may provide valuable information about electronic states, in the current study we targeted TAS spectroscopy as an approach to garner more information on radiative and non-radiative processes.

Broadband ultrafast DR spectroscopy

The time-delayed pump-probe DR-TAS data of a typical solution-processed CBTSSe sample (Figure 2D) is characterized by a weak tail at 680-725 nm, a narrow negative peak at 725-795 nm, and a positive spectrum formed at wavelengths above 807 nm. The intensity-dependent TAS studies are provided in Figure S4. As the results show, the ground-state bleaching (GSB) of CBTSSe is quite narrow and featureless, and the bleaching peak is spectrally located close to the band-edge absorption at 770 nm (shown in Figure 2C). The negative peak is assigned to GSB, and the positive absorption peak is assigned to ESA, which reflects the absorption by photogenerated minority carriers (see also the discussions of microscopy section). With increasing the pump power, the intensity of ESA increases (Figure S4). The ESA increase is linear (and not quadratic, for example). Therefore, one-photon absorption is involved (rather than multiphoton). This agrees with the intensity dependence TAM results discussed later. ESA is stable within the time frame of the experiments, which agrees with the ESA kinetics from TAM experiments (discussed later). We do not have evidence in our spectroscopy results pointing to exciton formation at room temperature. A near-band-edge exciton transition in PL of larger-band-gap CBTS films prepared by vacuum deposition was observed at a low temperature of 30 K. ¹⁷ The FWHM of the GSB peak is about 30 nm (67 meV, the data in eV units are provided in Figure S5), which is in agreement with that of previously measured vacuum-based CBTSSe samples.⁵

Using broadband spectroscopy measurements and analyzing the spectral shape and broadening of the peaks, it is possible to qualitatively deconvolute and compare different transient species when they are spectrally separated enough. For example, the bleaching caused by population within electronic trap states can be distinguished from the bleaching formed upon population at the band edge (or stimulated emission resulting from radiative recombination from these states) when they are spectrally (energetically) separated enough. However, the narrow GSB of CBTSSe makes spectral deconvolution difficult. Transient absorption microscopy provides the possibility to deconvolute and visualize the photoexcited species not accessible using ensemble spectroscopy.



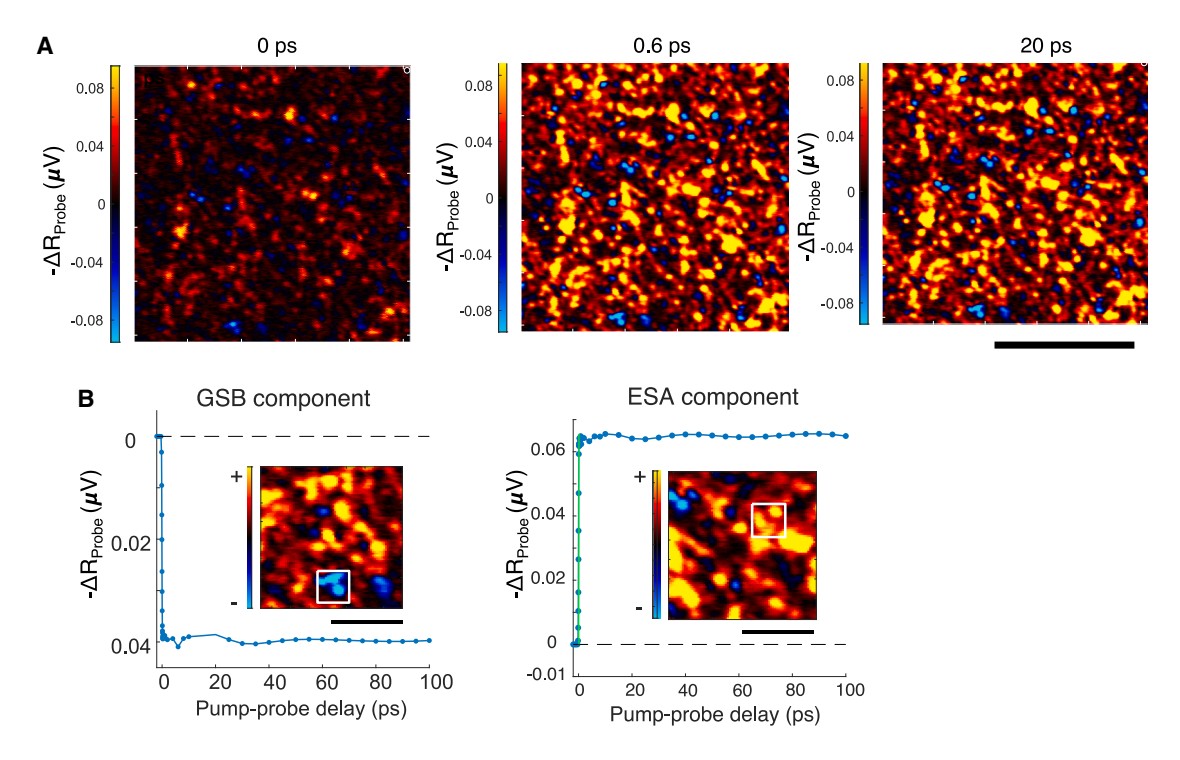


Figure 3. Stable ESA reflecting a stable charge carrier in solution-processed CBTSSe

(A) As an example, the pump-probe TAM image of the AA-0%-Na-CBTSSe film is shown at different time delays. The pump beam is 720 nm, and the probe beam is 820 nm. The scale bar represents 80 μ m. The pump-probe DR-TAM images are heterogeneously composed of negative and positive components over different grains.

(B) High-resolution scan over a relatively smaller area (48 48 μ m × 48 μ m) on the sample and TAS signals averaged over two regions of interest (shown in white boxes); one region identifies a negative GSB type of the TAS signal, and the other shows a positive ESA component. The scale bar represents 24 μ m, and the ROIs shown in the white box are 10 × 10 μ m.

Ultrafast two-color pump-probe DR microscopy of solution-processed CBTSSe

To deconvolute the photoexcited pattern and scrutinize the charge carrier formation and relaxation kinetics in solution-processed CBTSSe films, we performed two-color pump-probe experiments combined with confocal microscopy (pump-probe microscopy imaging), allowing localization and imaging of the ESA and charge carrier processes at a grain-scale level. In pump-probe DR-TAM, the pump-probe time delay is changed; at each delay point, a pump-probe TAM image (A = Pump_(on) – Pump_(off)) is acquired by scanning the pump and probe beams across the sample. The high repetition rate and sampling (see experimental procedures) enable TAS signal measurements with a high signal-to-noise ratio.

In Figure 3A, pump-probe images at different pump/probe time delays for the AA-0%-Na film are shown as an example. The three images correspond to different time delays, including the overlap time (0 ps) and after the overlap time (0.6 ps and 20 ps). The 720-nm pump beam, which has low energy while still being just above the bandgap, can penetrate deep into the sample and therefore allow monitoring of the charge carriers in the bulk of the film. For 820-nm photons, the penetration depth is about 1 μm , given the extinction at this wavelength.

Using broadband DR-TAS, the spectral positions of the ESA and GSB for CBTSSe films are determined (Figure 2D). The broadband spectrum is characterized by a positive TAS peak above 807 nm, which belongs to the ESA. Although the broadband spectrum can identify the spectral position of the ESA and GSB, with the



narrow and featureless shape of the GSB of the CBTSSe, it is not sufficiently versatile to enable an in-depth analysis of the electronic states, including the sub-band-edge states, and also to spectrally deconvolute the photodynamics.

In pump-probe microscopic imaging, we set the probe beam at 820 nm to access the positive TAS signal and monitor the free charge carrier dynamics. As observed, the pump-probe image heterogeneously comprises a dominant positive ESA component and a negative GSB component resolved at some grains. Conventional pump-probe spectroscopy experiments are typically performed on large ensembles of particles or molecules, where the response of individual contributors combines with that of others to produce strong optical signals. However, for some heterogeneous samples, the response from individual components is lost when averaging from across the ensemble. In the DR-TAM image of CBTSSe solution-processed samples, although the majority of the regions on the film represent a positive ESA signal, some grains show a negative GSB-type signal. Figure 3B shows a high-resolution scan over a relatively smaller area (48 μ m × 48 μ m) on the sample and the DR-TAM signal at two different regions. The pump-probe signal averaged over two regions of interest identifying ESA and GSB components is shown. The feature size in the pump-probe TAS images is in agreement with the SEM. Therefore, the pumpprobe images provide insight into the excitation pattern and the charge kinetics at the grain-size level. Notably, there is no change in the sign (positive or negative) of the signal. All negative-dominated grains remain negative throughout the time delay, while all positive-dominated regions remain positive. Therefore, the negative-positive pattern cannot be assigned to effects such as band gap renormalization resulting from charge accumulation (observed for perovskite materials³⁰) but rather to inherent electronic states. In general, a stimulated emission signal can be detected by pump-probe microscopy. The stimulated emission signal contrast would also result in an increased probe intensity at the detector (negative signal) same as GSB signal contrast (negative regions). However, our PL studies do not show any radiative recombination at 820 nm, and previous reports document that radiative recombination is not prevalent in CBTSSe materials at room temperature.²⁹

Also, we have to discuss the possible effect of film thickness variation on the pumpprobe TAS signal. The film surface is relatively smooth, although some voids are observed in the SEM (Figures 1 and S6), AFM (Figure S2), and PL images (Figure S3). Given that the depth of focus in our measurements is a few micrometers, such local variations are not sufficient to experience a defocused beam and a change in the intensity of the beam (Note S3).

Excitation-power dependence TAM studies

The effect of pump intensity on the pump-probe images and the TAS signal amplitude is depicted in Figure S7. With the increase in pump intensity, the TAS signal increase follows a linear trend, reflecting that signal formation does not arise from nonlinear absorption mechanisms such as two-photon absorption. Also, the increase in pump excitation does not affect the sign of the TAS signal of different grains, nor the averaged TAS signal from the entire scanned area; the grains with dominant GSB remain negative, and the grains with dominant ESA response remain positive. The advantage of microscopy over spectroscopy is that we can deconvolute the signal of individual components. The fluence dependence micro-spectroscopy is provided in Figure S8 (for excitation at 180, 450, and 800 μ W), with the extracted TAS signal of a typical negative grain labeled as a region of interest (ROI) shown as an example. By increasing the excitation power, the signal amplitude is enhanced, while the signal is stable within 100 ps. Therefore, the TR images and intensity-dependent measurements all confirm that the

Article



observed positive-negative pattern cannot be due to any local laser intensity variations, and it rather reflects the electronic variations (ESA and GSB) across the film. It should be noted that, in our control studies, the pump-probe images and the amplitude of the TAS signals were reproducible over consecutive measurements, indicating that no sample photodegradation occurred under this experimental condition (Figures S9 and S10; Note S4), and the technique is non-invasive.

For vacuum-deposited CBTSSe samples, we previously reported fast relaxation of ESA within a few picoseconds after excitation. For comparison, an example microspectroscopy measurement of a vacuum-deposited CBTSSe sample is provided in Figure S11 and discussed in Note S5. Figure S12 also shows an example intensity-dependent measurement on a CBTSSe vacuum-deposited sample. The TAS signals extracted from TAM images and over the ensemble of grains at different excitation powers (varying from 0.06–0.6 mW) are provided. The ESA relaxation kinetics are intensity dependent. For 0.06-mW excitation, the ESA signal's decay is fitted by a single exponential with a time constant of 433 ps and reaches a plateau at $\sim\!\!34\%$ of the signal. For 0.6-mW excitation, almost all of the ESA relaxes to zero, and the signal is fitted with a two-exponential decay function with time constants of 416 fs and 1.96 ps. Fitting parameters are provided in Note S6. The intensity-dependent relaxation kinetics confirm that relaxation of the TAS signal at 820 nm represents the relaxation (recombination) of free charge carriers in CBTSSe films.

Effect of Na incorporation and film processing on microscopic heterogeneity

Figure 4 compares the DR-TAM images of CBTSSe films 260 fs after excitation for different solution-processed samples, including 0%-Na-CBTSSe, 1%-Na-CBTSSe, AA-0%-Na-CBTSSe, and AA-1%-Na-CBTSSe. For all four samples, the DR-TAM is comprised of negative and positive features in different grains of the film, albeit with varying degrees of each of the components. Figure 4 clearly shows that, by Na doping and AA, the heterogeneity of the ESA-GSB is impacted. The most ESA-GSB heterogeneity (blue-red pattern) is observed for the as-deposited CBTSSe sample, and by Na doping, the number of blue regions is decreased, and the TAM image is relatively homogeneously comprised of ESA regions. DFT predictions for CZTSSe showed that Na energetically forms Na_{Zn} rather than Sn_{Zn} (known as a deep-level defect). ^{31–33} Hence, Na doping is able to suppress formation of detrimental Sn_{Zn} defects and has been observed to improve device performance. ³⁴ Interestingly, the current data suggest that TAM microscopy offers a way to directly visualize the effect of varying solution processing, including doping and annealing, on the heterogeneity of defects and passivation in the film.

In Figure S13, the pump-probe TAS signal averaged over the entire scanned area appears next to each pump-probe image. Remarkably, the TAS signal is flat over 100 ps with no decay observed, which indicates that the charge carriers are stable within this time frame. In our previous measurements on vacuum-based sputtered CBTSSe samples, paperoximately 80% of the TAS signal (ESA component) decayed in a few picoseconds, while the remainder had a long lifetime with a flat signal over hundreds of picoseconds. In other words, the majority of charge carriers were trapped or recombined in a few picoseconds after excitation, and the remainder were stable. Here, we did not observe the picosecond relaxation component for the solution-processed samples; one important conclusion is, therefore, that the preparation method has a noticeable influence on the film's optoelectronic characteristics. Namely, we observed that the free charge carriers are stable in solution-processed films, which is particularly important for integration of this material family in energy conversion applications and solar cell devices. The long-time-delayed kinetics of



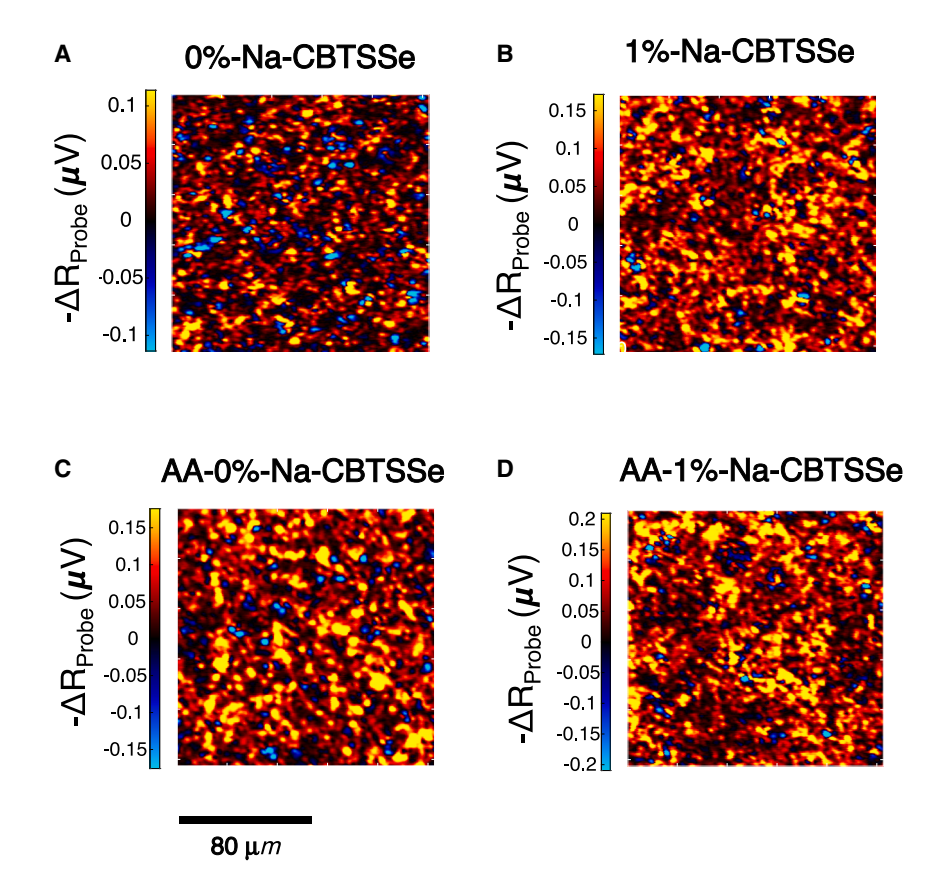


Figure 4. Effect of Na doping and air-annealing on the heterogeneity of the pump-probe DR-TAM of solution-processed CBTSSe films

(A–D) 0%-Na-CBTSSe (A), 1%-Na-CBTSSe (B), AA-0%-Na-CBTSSe (C), and AA-1%-Na-CBTSSe (D). The pump-probe TAS image shown is at 260 fs. The pump beam is 720 nm, and the probe beam is 820 nm.

charge carriers in CBTSSe films were measured using TR terahertz spectroscopy.²⁹ Terahertz spectroscopy is sensitive to the number of free carriers and their associated mobility. This earlier study on similarly prepared samples observed a long decay tail with a lifetime of 2.5 ns when the sample was excited at 800 nm. This is in agreement with our measurement.²⁹

Quantified two-color pump-probe TAM image analysis

For quantified analysis of images, and scrutiny of the heterogeneity pattern, we applied different image analysis methods.

Pixel-based statistical analysis

To deconvolute the photoexcited pattern across the film, histogram analysis is performed. The image histogram chart shows the distribution of intensities in the image. In this analysis, the frequency of pixels for each color-coded region of the colormap (which represents the signal sign and intensity) is defined. The histogram analysis is done using a standard Parula colormap, which provides better contrast for visualization of the zero-signal regions and the TAS signal. The histogram charts of the pump-probe images of two different CBTSSe samples are shown in Figure 5. The two overlaid histogram charts are also shown in Figure S14. Figure 5, left, shows the Parula color-coded TAM images. In Figure 5, right, the histogram of the entire colormap for each sample is shown. For both samples, the frequency of the ESA regions is higher than the



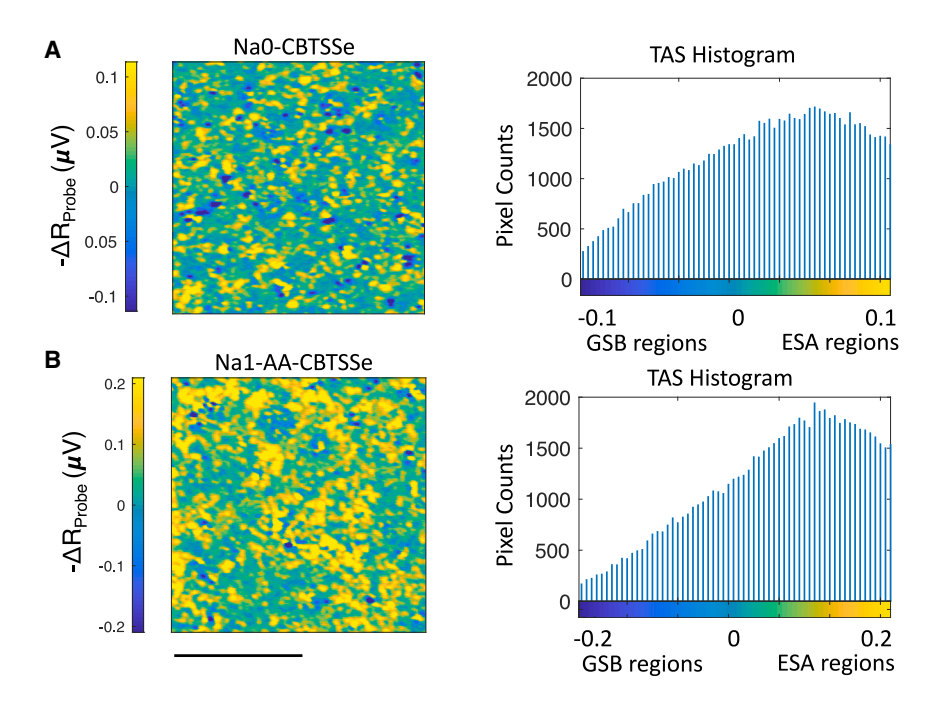


Figure 5. Histogram analysis of the TAS signal extracted from pump-probe images of CBTSSe samples for quantification of heterogeneity in doped versus undoped films

(A and B) Na0-CBTSSe (A) and Na1-AA-CBTSSe (B). This analysis is done on the Parula standard colormap applied on the pump-probe image, shown on the left. The scale bar represents $80\,\mu m$. On the right, the histogram of the entire colormap (which reflects all signal intensities) for each sample is shown. The positive region and negative region are labeled with ESA and GSB, respectively. Substantial differences are observed in the TAS histogram chart of 0%-NA- CBTSSe and 1%-Na-AA-CBTSSe samples. For both samples, the number of the ESA regions is higher than the number of the GSB regions. By Na doping and AA, the GSB region is further diminished. Significantly, in 0%-Na CBTSSe samples, the number of GSB regions is higher (by 27%) and the number of positive regions is slightly lower than in 1%-Na-AA-CBTSSe. Also, the number of zero regions is higher in 0%-Na CBTSSe compared with 1%-Na-AA-CBTSSe.

frequency of the GSB regions. Substantial differences are observed in the histogram chart of 0%-Na CBTSSe and 1%-Na- AA-CBTSSe samples. Remarkably, the number of GSB regions in 0%-NA-CBTSSe samples is 27% more than in 1%-Na-AA-CBTSSe. The number of ESA regions is less in 0%-Na-CBTSSe than that in 1%-Na-AA-CBTSSe. The number of zero regions is more in 0%-NA-CBTSSe compared with 1%-Na-AA-CBTSSe. This analysis shows that a number of regions do not effectively generate any signal in pristine 0%-Na CBTSSe samples and that sample treatment (AA and Na doping) has enhanced the effective charge carrier generation in the CBTSSe films. The GSB resolved at 820 nm is assigned to carriers localized within sub-band-gap trap states (see the extended model in the discussions). The histogram analysis agrees with PCA data analysis (discussed later), in which we observed that the negative signal coverage was weaker on 1%-Na-AA-CBTSSe compared with pristine 0%-Na CBTSSe, and both reflect that the Na doping-AA process on the sample has considerably decreased the charge carrier trapping (charge carriers are less localized in the electronic states in the Na-AA-treated sample by 27%).

The contributions of the negative GSB and positive ESA in the TAS image of the four different samples (shown in Figure 4) are provided separately in Table 1. To define the ESA regions (all positive regions) and GSB regions (all negative regions), a threshold value is set. According to the image colormap, yellow/red regions



Table 1. Effect of Na additive and air-annealing on the ESA and GSB pattern resolved by DR-TAM for different solution-processed CBTSSe samples

	CBTSSe 0% Na	CBTSSe 1% Na	CBTSSe 0% Na, AA	CBTSSe 1% Na, AA
Percentage of the GSB in the TAS signal	35%	27%	28%	12%
Percentage of the ESA in the TAS signal	65%	73%	72%	88%

correspond to positive regions, and light/dark blue correspond to GSB regions. The black regions correspond to zero signal. The noise level is considered the threshold value, and the signal at each pixel (region) is compared with that. In Figure S15, examples of ESA, GSB, and zero signals are shown (also consider the description in Note S7). The values in this table represent the percentage of contributions of the ESA and GSB to the total TAS signal measured over all the grains of each sample. Notably, Na addition and AA decreased the GSB contribution and increased the ESA contribution in the TAM images and TAS signal measured over all grains.

We hypothesize that chemical composition variation is responsible for the observed longer carrier lifetime. To scrutinize the chemical composition of the samples, we performed X-ray photoelectron spectroscopy (XPS) analysis on solution-processed films: Na1-CBTSSe with and without AA. The XPS spectra at Sn 3d and Se 3d core-level positions are shown in Figure 6. The XPS spectra of CBTSSe films before

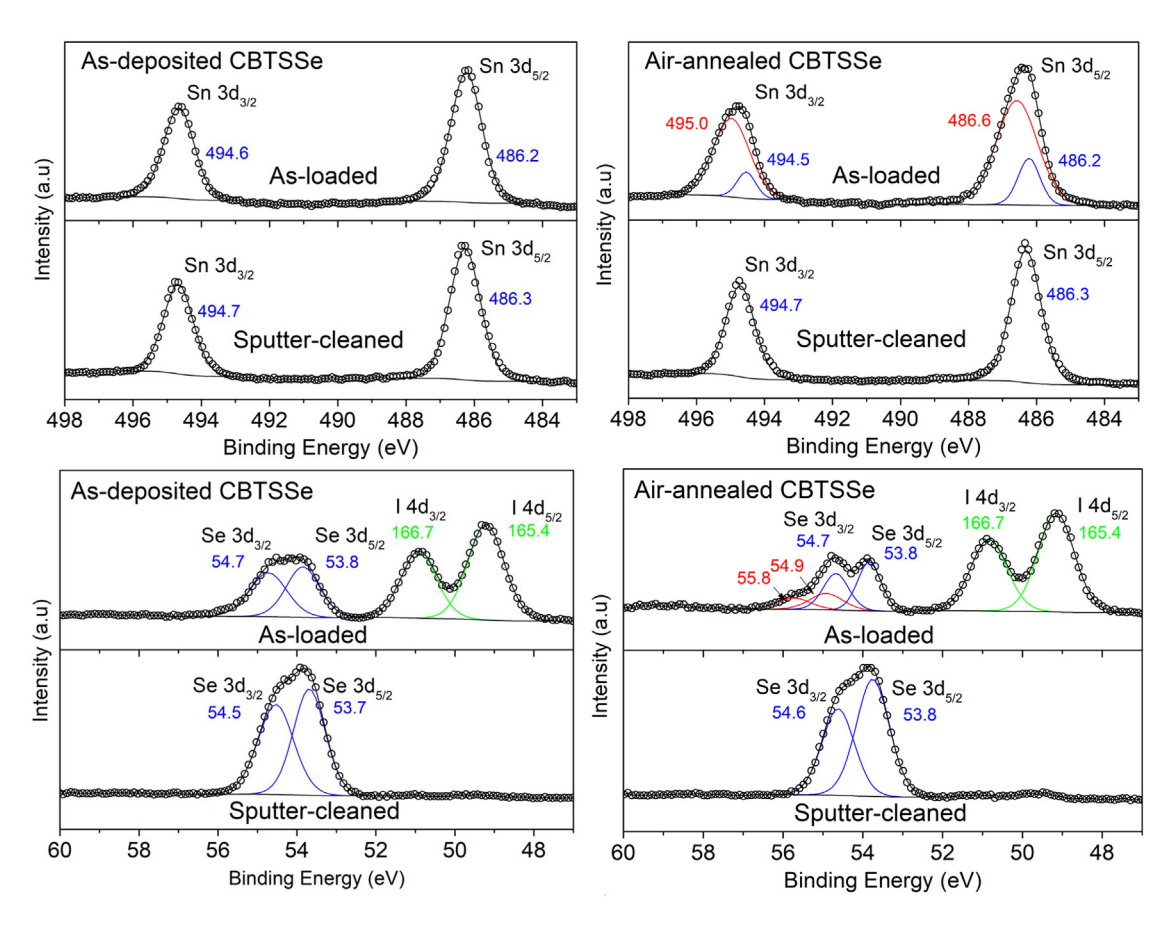


Figure 6. XPS spectra of Na1-CBTSSe before and after air-annealing

Shown are XPS spectra of Sn 3d and Se 3d core-level positions of CBTSSe films (left) before and (right) after AA treatment. Sputter cleaning was performed using 5-kV Ar ions. Open symbols, measured data; black solid lines, enveloping curves and backgrounds; colored curves, fitted peaks.

Article



and after AA treatment reflect oxidation of the film surface. XPS spectra near the Sn 3d peak of the air-annealed CBTSSe films exhibit a noticeable broadening of peaks toward higher binding energy that reflects increased oxidation states of Sn (SnO_x with $x \approx 1.65$). On the contrary, there are no significant changes in peak positions and widths of Cu 2p and Ba 3d core-level peaks before and after AA treatment (see Figure S16 and the XPS discussions provided in Note S8), implying that the AA treatment primarily causes oxidation of Sn, which is also observed for CBTS³⁶ and CZTS. 37,38 Sn oxidation is known to be beneficial for CZTS devices because the SnO_x secondary phase forms a type I band offset with CZTS at grain boundaries, which has been shown to improve device performance by suppressing recombination of charge carriers.³⁷ Further, in as-deposited and air-annealed samples, additional S 2p peaks at 165.4 and 166.4 eV appear (Figure S16, green curves), indicating the presence of ${\rm SO_4}^{2-.17}$ This observation agrees with backscattered electron SEM (Figure S6), which shows the presence of the BaSO₄ phase (below the detectable level for XRD) at the CBTSSe film surface and grain boundaries. Therefore, the XPS results point to secondary phase formation (BaSO₄ and SnO_x).

Principal-component analysis

We performed principal-component analysis (PCA) of the pump-probe TAM images of different CBTSSe samples. In the PCA, we identify a set of orthogonal basis TAS signal components, called principal components (PCs), that can be combined to reproduce the signal at any given pixel. The proportion of PCs found in each pixel can be used for further analysis.³⁹ The data collected are in the form of a threedimensional data cube (x, y, and t); x and y are spatial dimensions (pixels), and t reflects the temporal evolution. The main components are defined by analyzing the signal for each pixel (512 x 512) in a way that the signal vector for each pixel can be approximated by a non-negative linear combination of component vectors (PC). The signal vector at one spatial pixel can be expressed as $si = \Phi \nu i + \varepsilon i$, where Φ and ν i are the components and mixing coefficients of the components, respectively, and ε i is the noise/approximation error. The components are defined simply through this algebra tool to represent the best vectors that, when added, give the best representation of the experimental data with minimum approximation error. Other combinations of components' vectors could be possible but do not minimize the residual/approximation error. The PCAs of the 0%-Na-CBTSSe and AA-1%-Na-CBTSSe films are shown for comparison in Figure 7. For both samples, the representative false-color images rendered from PCA of the pump-probe images and images of each PC are shown. The PC signals are provided. The actual pump-probe image acquired at 260 fs is also demonstrated for comparison. This analysis shows that the pump-probe TAM images can be constructed by three PCs, two of which contribute to the transient pump-probe response (one positive and the other negative). The third component is an instantaneous signal that only appears at the overlap time of the pump and probe (zero time), and its time duration is within the time resolution of our technique. This instantaneous signal is assigned to nonlinear optical processes and is not suitable for dynamic analysis in our samples.

It is also important to compare the PCA of two CBTSSe samples; one sample without AA and Na doping and the other with AA and Na doping. As can be seen in the corresponding figures for PC1 and PC2, positive and negative components are distributed across different grains of the film. This important observation indicates that, for example, for regions that appear solid blue in the TAM images, basically, the negative component mainly dominates the positive, while both components can be present. This analysis is of particular importance for understanding the nature of the heterogeneity in photoexcited patterns of CBTSSe films. By looking at the TAM images, one might think that only



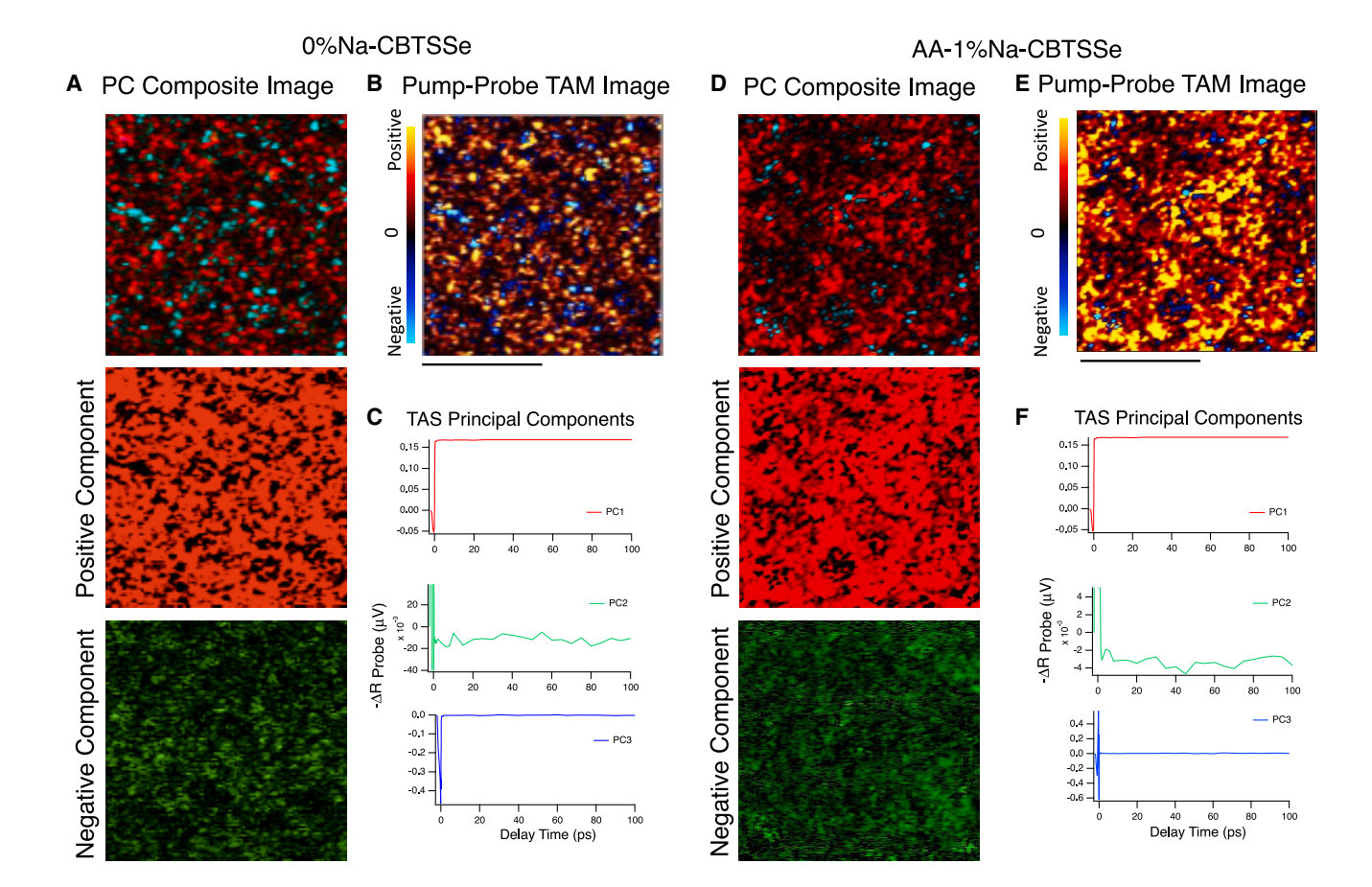


Figure 7. Principal component analysis of the pump-probe TAM image of the 0%-Na-CBTSSe and AA-1%-Na- CBTSSe films

(A and D) Representative false-color images of PC1 (red) and PC2 (green) and the composite image (green and red) obtained by projection of PCA on the pump-probe image of the sample.

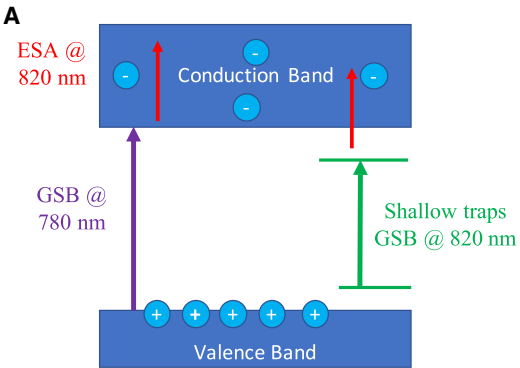
(B and E) The pump-probe TAM image is shown for comparison. The pump-probe TAM image can be reproduced by two PC images. Positive and negative components are distributed across different grains of the film. The positive component is stronger than the negative component. (C and F) The corresponding three PC signals are depicted. PC1 and PC2 contribute to the time-delayed TAS signal and are considered for our analysis, while PC3 is an instantaneous signal that appears at the pump and probe overlap time within the time resolution of our technique. The scale bar represents 80 µm.

certain grains are negative. However, these data show that blue colors (bleaching type of signal) do not belong only to specific grains, but, rather, they are distributed over different grains of the film with a different amount.

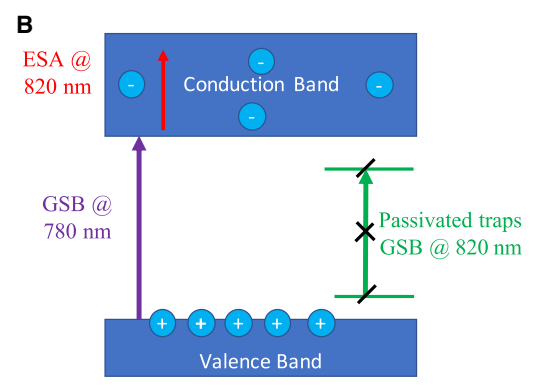
For 0%-Na-CBTSSe and AA-1%-Na-CBTSSe, the positive component is stronger than the negative component. The negative component is further diminished in AA-1%-Na-CBTSSe. The PCA results, together with the pump-probe TAM image statistical analysis, confirm that, by solution processing, Na doping and AA, the ratio of the positive component (ESA) to the negative component (GSB because of charge carriers localized in sub-band-gap states) is increased considerably.

In the broadband ensemble spectroscopy measurements (Figure 2D), at 820-nm probe wavelength, the positive ESA is observed in the TAS signal (with a sharp cut-off from the narrow GSB component observed around 780 nm). In the two-color pump-probe TAM images, measured at 820 nm, the majority of grains show a positive ESA signal, and the TAS signal averaged over the entire scan area is positive,





Presence of shallow traps (bandgap variation) results in positive-negative heterogeneous TAM image.



Shallow trap passivation results in positive signal dominated homogeneous TAM image.

Scheme 1. Schematic of the effect of band-gap variation via shallow trap state formation and passivation on the expected DR-TAM image The band gap of the CBTSSe is 1.6 eV.

(A) The presence of shallow traps can localize carriers at energies below the band gap. Therefore, a heterogeneous negative-positive TAM image is expected at the 820 nm probe, where the positive component represents the ESA by the minority carrier in the conduction band or from the trap states, and the negative component represents bleaching because of carriers localized within sub-band-edge states.

(B) Passivation of shallow traps decreases the bleaching component, which results in a more homogeneous TAM image with dominating positive ESA.

while in some grains, a negative signal is observed. Importantly, all data analyses support that the contribution and heterogeneity of the positive and negative components are different in different CBTSSe solution-processed samples. Using PCA, we could deconvolute the two kinetic components and map each component in a separate image. Using histogram analysis, we can define the ratio of the regions with no signal to the active regions with a transient photoresponse. Importantly, the PCA unravels that the negative component is distributed over entire grains with different contributions rather than being restricted to some grains. The PCA, together with the pump-probe images, confirms that the contribution of positive outweigh the weak negative signal in most grains and that the negative regions are even more diminished in the air-annealed and Na-doped samples. The statistical analysis also shows that the percentage of the active regions to the zero-signal regions is increased in air-annealed and Na-doped samples compared with the pristine CBTSSe sample. Notably, all results presented in this paper are achieved by performing several sets of measurements and iterations on different samples, different regions on the same sample, and, in general, under different experimental conditions to ensure the reproducibility of the reported trend. In Figures S17 and S18, the experimental results of pump-probe measurements and histogram analysis of another sample under Na1-AA-CBTSSe experimental conditions are shown. By comparing the histogram results with those reported in Figure 7, we observe that the same trend is supported (see also Note S9 for data trend reproducibility).

To understand the effect of solution processing on the TAM images, we should note that the presence of GSB-dominated regions in TAM images can be a sign of any parameter that has resulted in energy level variation (Scheme 1A). This variation can be caused by different parameters, including small S/Se ratio stoichiometry variations that result in red/blueshift of the absorption spectrum⁶ or the presence of shallow traps that can localize charge carriers in the sub-band-gap states (with an effect similar to band-gap narrowing). We have to rule out S/Se stoichiometry variations in different films because of several experimental observations;



namely, the results of PL and UV-visible (UV-vis) absorption, supported by XPS. According to the PL analysis, solution processing has not macroscopically changed the band gap of different CBTSSe films because the PL of all four samples is centered at the same wavelength. The S/Se variations would result in a shift in the PL spectrum.⁶ We did not observe any spectral shift in the PL or in the optical absorption edge of the samples. Therefore, it is unlikely that the type of solution processing applied to different films (Na addition or AA) will significantly change the S/Se stoichiometry. Our experimental and data analysis results all point to the effect of sub-band-gap electronic states. The presence of shallow traps and a slight band tailing could result in a locally narrower effective band gap. This can also explain the distribution of the negative component with different amounts over different regions of the sample so that, at 820 nm, some regions represent a stronger bleaching type of signal (Scheme 1A). The density of shallow traps could be affected by solution processing and post-processing. The weaker negative component in the AA-Na1-CBTSSe sample compared with the pristine Na0-CBTSSe can be due to passivation of such sub-band-edge trap states. With trap passivation, the bleaching signal decreases, and, therefore, the ESA contribution relative to GSB is increased in the TAM image (Scheme 1B). Therefore, in our pump-probe microscopy imaging measurements, GSB represents the carriers localized in the sub-band-edge states. We can conclude that Na addition and AA have a considerable effect on the existence of localized versus free charge carriers. In other words, with Na incorporation and AA, the population of free carriers over the carriers localized in near-band-edge traps is enhanced, which is a useful observation from a device engineering point of view.

Shallow trap states at 820 nm (1.5 eV) (near band edge) have also been detected experimentally using low-temperature (LT) PL experiments on samples prepared similarly as those in the current study.²⁹ In the LT PL measurement, the peak at 1.5 eV (820 nm) belongs to radiative recombination from defects level. The negative 820 nm (1.5 eV) pattern in the TAM measurements at room temperature may be attributed to the population (GSB) of these levels. Shallow defects and deep defects levels are also reported by LT PL experiments for larger-band-gap CBTS analog materials. The same 1.5-eV defects level are present for the larger-band-gap CBTS phase. The 1.5-eV level is considered a deep level for the CBTS phase (bigger distance from the band edge).⁴⁰

Remarkably, the lifetime of the charge carrier is enhanced in all CBTSSe films made by the solution synthesis method compared with our previously reported CBTSSe films prepared by sputtering.⁵ Also, the heterogeneity of the TAM images is less than that of the vacuum-deposited films. For comparison, a typical pump-probe result of the CBTSSe vacuum-deposited film measured at identical conditions is shown in Figure S11. It has been proposed computationally⁴¹ that the chemical potential during synthesis impacts defect formation energy. It can be expected that the synthesis method would impact the defect chemistry and, therefore, the photophysics. The different defect densities will lead to different spectroscopic behavior. Our experimental results are consistent with the conclusion that secondary phase formation (large-band-gap SnO_x and BaSO₄) and shallow trap passivation may underlie the longer carrier lifetime and more homogeneous excited state pattern in CBTSSe films prepared using the described solution processing approach compared with previously studied vacuum-deposited films. The Na additive may passivate the shallow traps close to the band edge, which can cause energy variations in different grains across the film. According to the XPS analysis (Figures 6 and S16), AA causes surface Sn oxidation and formation of SnO_x with $x \approx 1.65$. SnO_x formation at grain boundaries can supposedly passivate shallow trap states as well. It is noteworthy

Article



that it has been determined previously that SnO_x formation on CZTSSe samples forms a type I band offset with CZTS at grain boundaries. From a device perspective, it has been observed that AA of CIGSSe and CZTSSe films improves solar device performance. $^{6,34,42-44}$ Formation of the secondary $BaSO_4$ phase on the film and on the grain boundaries (Figure S5) can also be a possible mechanism for the longer lifetime observed in the solution-processed films. $BaSO_4$ nanocrystals have a large band gap (band gap in UV). Therefore, formation of these large-band-gap crystals possibly inhibits charge recombination by building an energy potential wall (band offset). It should be noted that the large-band-gap $BaSO_4$ is not interacting with the 720-nm excitation, so the TAS signal reflects direct excitation of CBTSSe.

It is reasonable to discuss the relevant reported PV performance of CBTSSe films and future potential for improvements. Given that the band gap of the CBTSSe film is 1.59 eV, the Shockley-Queisser (SQ) limit predicts a maximum achievable value of open circuit voltage (V_{oc}) for this absorber of \sim 1.31 V. By measuring the PL quantum yield on similarly prepared CBTSSe films at high excitation intensities and extrapolating under 1-sun conditions, the quasi-fermi level splitting is estimated to be 0.68 eV, and therefore, the contribution of non-radiative recombination to V_{oc} loss can be considered to be \sim 0.62 V. The best thin-film solar cell device in this earlier study provided a V_{oc} of 0.47 V, which is only about 36% of the V_{oc} predicted by the SQ limit. More recent record devices with improvements in device design offer a power conversion efficiency of 6.2% and a V_{oc} of 0.68 V. Several factors contributing to suboptimal device performance may include a low minority carrier lifetime and mobility (associated with a significant concentration of bulk and/or surface defects) and low-concentration charge carriers. 9,45

It is significant that the sensitivity of the pump-probe DR microscopy measurements would provide a tool to relate the fine chemical composition to the spectroscopic behavior of the sample. Particularly, it has been a challenge for the field to find fingerprints of the trap states in such TR spectroscopy and deconvolute the photodynamics of different transient species with overlapping spectral absorption. Accordingly, using ultrafast broadband DR-TAS and two-color DR-TAM, we analyzed the photophysical processes, including the kinetics of charge carrier processes within electronic and trap states, of solution-processed CBTSSe samples. The unique sensitivity of the spectroscopy and microscopy methods allows localizing the ESA pattern and charge carrier kinetics across the film grains and within trap states. There are several important points to consider regarding pump-probe microscopy of the solution-processed samples. First, the charge carrier kinetics are remarkably improved for all solution-processed films compared with vacuum-deposited samples, with charge carriers being stable until hundreds of picoseconds. The observed enhancement in the charge carrier lifetime is of particular importance for integration of these films in energy conversion applications, including solar cell devices. Second, our experimental results show that the heterogeneity in the TAS images of the solution-processed samples is less than that in vacuum-deposited samples (as reported previously⁵). Third, by changing the solution processing parameters, such as Na addition and/or AA, the heterogeneity tends to decrease (the pump-probe TAM image is more positively dominated). We integrated the PCA and histogram analysis, and the results show that the amplitude of the negative signal component and the number of non-active regions that do not generate a TAS signal, is diminished in the sample with AA and Na doping compared with the pristine sample.

The spatial and spectral GSB/ESA heterogeneity can be due to the existence of shallow traps, which cause energy variations and band tailing, according to our



optoelectronic model (Scheme 1). The observed decrease in the GSB/ESA heterogeneity upon film processing (Na addition and AA) is assigned to trap state passivation. The Na additive could passivate the shallow traps close to the band edge, which can cause energy variations in different grains across the film. Passivation of the traps can result in more homogeneous positive-dominated pump-probe images, as discussed for the optoelectronic model. It is also plausible that the secondary phases consisting of the large-band-gap $\rm SnO_x$ and $\rm BaSO_4$ that are formed during solution processing of the film can build up local energy barriers that can reduce charge carrier recombination at interfaces.

The ultrafast photophysical analysis discussed here is also significant in the sense that pump-probe microscopy facilitates resolving and spatially locating different excitation patterns within the film, enables localizing the minority component in the TAM images (GSB signal), and provides a microscopic relation between the compositional/energy variations to the ultrafast photophysics at the grain size level in the film.

EXPERIMENTAL PROCEDURES

Resource availability

Lead contact

Requests for further information should be directed to the lead contact, Elham Ghadiri (ghadire@wfu.edu).

Materials availability

This study did not generate new unique materials.

Data and code availability

The published article and its supplemental information include all data generated or analyzed during this study.

Molecular ink synthesis and film formation

A molecular solution was prepared using the commercially available precursors Cu(CO₂CH₃)₂ (98%, Sigma-Aldrich), anhydrous SnI₂ (99.99%, Sigma-Aldrich), Ba(NO₃)₂ (99.99%, Sigma-Aldrich), thiourea (NH₂CSNH₂) (≥99.0%, Sigma-Aldrich) and NaCl. Solution preparation and film formation temperatures were modified slightly relative to our previously indicated temperatures and solution preparation steps.⁸ Prebake, sulfurization, and selenization temperatures were set to 580°C, 590°C, and 580°C, respectively, using a homemade hotplate. The molecular stoichiometry of the initial solution was maintained using 2.56/1.28/1.92/5.38 mmol of Cu/ Sn/Ba/thiourea (i.e., nominally Ba and S rich relative to the ideal stoichiometry of CBTS). Cu/Sn and Ba/thiourea precursors were mixed separately in 2 mL DMSO (99.99%, anhydrous, Sigma-Aldrich) and stirred overnight at room temperature. Ba/thiourea precursor solution was mixed with Cu/Sn precursor solution to prepare the non-additive ink. To prepare Na additive ink, NaCl was added to Ba/thiourea precursor solution and then mixed with Cu/Sn solution. The atomic ratio of Na in the Na additive ink was calculated as Na/(Cu+Ba+Sn) = 0.01 (1%) (atomic ratio of Na to all metal ions). All steps described in this section were conducted in an N₂filled glovebox. AA of CBTSSe/Mo/SLG samples was done at 200°C for 2 min under ambient conditions.

Pump-probe DR microscopic imaging and spectroscopy

The two-color pump-probe system used a part of the fundamental beam to pump a tunable, intracavity frequency-doubled, optical, parametric oscillator, used as

Article



the pump beam for the experiments. The pump beam was set at 720 nm. A second beam at 820 nm was used as the probe beam. The bandwidth of the pump and probe pulses was 5 nm. The time resolution was defined by measuring the two-photon absorption cross-correlation in rhodamine-6G, about 250 fs. The pump beam and the probe beam were sent collinearly into a home-built microscope. The microscope was fitted with a 20× objective. In reflectance mode measurements, the diffuse reflected pump beam was directed to the detector. Appropriate chromatic filters were applied just before the detector to reject the pump beam. A lock-in amplifier amplified the signal and measured the modulation passed from the pump beam to the probe beam ($Sig(\mu V) = -\Delta R_{Probe} = R_{Probe unpumped} - R_{Probe pumped}$). By convention, positive signal refers to ESA (i.e., less probe intensity at the detector), and negative refers to less probe absorption by the sample (more probe intensity at the detector). Regular imaging conditions were around 0.6 mW for each beam, measured on the sample, corresponding to 0.3-nJ pulse energy.

For the transient absorption spectroscopy measurements, the pump beam at a defined wavelength is produced. The pump is modulated using a synchronized chopper for pump on/pump off experiments. In the broadband TAS spectrum, the y axis is absorbance change, defined from the equation $Sig = \Delta A = -Log(\frac{lp}{lu})$, where I_p and I_u refer to the intensity of the probe at detector with and without pump excitation, respectively. The pump beam has a radius of about 100 μm at the surface of the sample. The typical power of the pump is about 100–600 μW or 318-1,910 mW/cm², giving an energy fluence of 0.6-3.8 mJ/cm². The probe beam is a white-light continuum generated in a sapphire plate (2 mm thick), having less energy than the pump on the sample to avoid multiple excitations. The probe beam is focused onto the sample with a spot size of around half of that of the pump (i.e., about 27 μ m). The typical power on the sample for the probe beam is from 16–20 μ W, giving an energy fluence of 2.8–3.5 mJ/cm². The pump and probe beam are irradiated onto the sample, and the diffuse reflected probe beam is collected, collimated, and focused into the detector. The pump beam entrance to the detector is blocked by using appropriate band pass filters and cutoff filters, and the white light probe beam is recorded. The polarization of the pump and probe pulses was set at the magic angle of about 54° to consider all polarizations in the sample.

PL imaging and UV-vis absorption spectroscopy

Steady-state PL imaging of the samples was performed using a Carl Zeiss LSM 880 confocal microscope. The optical absorptance spectrum of samples was measured by a PerkinElmer UV-vis spectrophotometer equipped with an integrating sphere (PerkinElmer Lambda 950 and 100 mm sphere). Because the samples are opaque and deposited on Mo metal substrate, the DR is measured. The Kubelka-Munk spectrum is calculated from $(F(R) = \frac{(1-R)^2}{2R})$.

Thin-film characterization

The film-phase homogeneity was assessed with XRD patterns using a PANalytical Empyrean powder X-ray diffractometer and Cu K α radiation. Top and cross-section SEM images of CBTSSe films were taken using an FEI XL30 SEM system with 5-kV and 10-kV accelerating voltages, respectively.

Elemental concentrations of metal precursors were determined by acid digestion followed by analysis with ICP-MS (Agilent 7900). The CBTSSe film deposited on Mo-coated SLG substrate was dissolved by sequentially dropping 1.6 mL HNO $_3$



(ACS grade) and 0.4 mL HCI (ACS grade) acids into a beaker and allowing enough time for dissolution of the CBTSSe film from the Mo-coated SLG substrate. The solution was then further diluted with 20 mL of DI water. A reference sample, including only HNO₃, HCl, and DI, was also prepared with the same volume ratios for the measurement. Analysis of all elements was carried out under a He atmosphere (collision cell) to reduce polyatomic interference. All standards and samples were diluted into a 2% $HNO_3/0.5\%$ HCl (v/v) (Fisher Scientific trace metal grade) matrix made with 18.2 $M\Omega$ water prior to analysis. The instrument was calibrated for 23 Na, 63 Cu, 138 Ba, and 119 Sn prior to sample analysis (0.1–250 μ g/L for Cu, Ba, and Sn; 25-250 μg/L for Na) using a Spex Certiprep standard containing Na, Cu, and Ba (mixed element 2A) with an addition from a single-source Spex Certiprep Sn standard. ⁴⁵Sc, ⁸⁹Y, ¹⁰³Rh, ¹¹⁵In, and ¹⁵⁹Tb were used as internal standards to correct for shifts in the analyte signal intensity during the analysis run. The calibration was verified using NIST traceable second source standards. For Na, Cu, and Ba, a standard (CRM-TMDW-A) from High Purity Standards was used, while a standard purchased from Agilent was used for Sn. The digested samples were diluted by a factor of 50 or 10,000 to ensure that the analytes of interests were within the calibration curve.

TOF-SIMS analyses were conducted using a TOF SIMS V (Ion TOF, Chestnut Ridge, NY, USA) instrument equipped with a Bi_n^{m+} (n = 1–5, m = 1, 2) liquid metal ion gun, Cs⁺ sputtering gun, and electron flood gun for charge compensation. Both the Bi and Cs ion columns were oriented at 45° with respect to the sample surface normal. The instrument vacuum system consisted of a load lock for rapid sample loading and an analysis chamber, separated by a gate valve. The analysis chamber pressure was maintained below 5.0 \times 10⁻⁹ mbar to avoid contamination of the surfaces to be analyzed. For high-mass-resolution spectra acquired in this study, a pulsed Bi₃⁺ primary ion beam at 25 keV impact energy with less than 1-ns pulse width was used. An electron gun was used to prevent charge buildup on the insulating sample surfaces. The total accumulated primary ion dose for data acquisition was less than 1 \times 10¹³ ions/cm², a number of ions within the static SIMS regimen. The mass resolution on the Si wafer was \sim 8,000 m/ Δ m at 29 AMU. For depth profiles acquired in this study, 10-keV (or 3-keV) Cs⁺ with 30-nA current was used to create a 120 \times 120- μ m sputtered area, and a 50 \times 50 μ m area was analyzed using a 0.3-pA Bi₃⁺ primary ion beam. The positive ion spectra were calibrated using O+, Na+, Mg+, Al+, Cu+, Mo⁺, Sn⁺, and Ba⁺ ions.

The surface morphology was characterized by AFM using an Asylum Cypher atomic force microscope. XPS spectra were acquired using Kratos Analytical Axis Ultra with a monochromatic Al K_{α} (1,486.6 eV) as the X-ray source. Sputter cleaning of the film surface was conducted using a focused Ar⁺ beam with an accelerating voltage of 5 kV.

SUPPLEMENTAL INFORMATION

Supplemental information can be found online at https://doi.org/10.1016/j.xcrp. 2023.101601.

ACKNOWLEDGMENTS

E.G. acknowledges financial support from NSF (CHE) under award 2239539. H.L., A.S., and E.G. appreciate H. Brown-Harding of the WFU microscopy unit and J. Kassis of WFIRM. B.T., Y.K., and D.B.M. acknowledge financial support from the US DOE, Basic Energy Sciences (BES), under contract DE-SC0020061.

Article



AUTHOR CONTRIBUTIONS

H.L. acquired PL imaging/spectroscopy and analyzed the PL and pump-probe data. A.S. acquired parts of the UV-vis data and helped with the MATLAB coding. B.T. prepared samples and performed structural characterization. Y.K. performed XPS analysis. D.B.M. instructed materials preparation and structural characterization. E.G. contributed the project idea, ultrafast experimental design and data acquisition, and time-resolved data analysis and wrote the manuscript. All authors read and agreed to the manuscript prior to submission.

DECLARATION OF INTERESTS

The authors declare no competing interests.

Received: October 16, 2022 Revised: July 18, 2023

Accepted: September 6, 2023 Published: September 28, 2023

REFERENCES

- Green, M.A., Dunlop, E.D., Levi, D.H., Hohl-Ebinger, J., Yoshita, M., and Ho-Baillie, A.W.Y. (2019). Solar cell efficiency tables (version 54). Prog. Photovoltaics Res. Appl. 27, 565–575. https://doi.org/10.1002/pip.3171.
- Gokmen, T., Gunawan, O., Todorov, T.K., and Mitzi, D.B. (2013). Band tailing and efficiency limitation in kesterite solar cells. Appl. Phys. Lett. 103, 103506. https://doi.org/10.1063/1. 4820250
- Sun, J.-P., McKeown Wessler, G.C., Wang, T., Zhu, T., Blum, V., and Mitzi, D.B. (2020). Structural Tolerance Factor Approach to Defect-Resistant I₂-II-IV-X₄ Semiconductor Design. Chem. Mater. 32, 1636–1649. https:// doi.org/10.1021/acs.chemmater.9b05107.
- Zhu, T., Huhn, W.P., Wessler, G.C., Shin, D., Saparov, B., Mitzi, D.B., and Blum, V. (2017). I2– II–IV–VI4 (I = Cu, Ag; II = Sr, Ba; IV = Ge, Sn; VI = S, Se): Chalcogenides for Thin-Film Photovoltaics. Chem. Mater. 29, 7868–7879. https://doi.org/10.1021/acs.chemmater. 7b02638.
- Ghadiri, E., Shin, D., Shafiee, A., Warren, W.S., and Mitzi, D.B. (2018). Grain-Resolved Ultrafast Photophysics in Cu₂BaSnS_{4-x}Se_x Semiconductors Using Pump-Probe Diffuse Reflectance Spectroscopy and Microscopy. ACS Appl. Mater. Interfaces 10, 39615–39623. https://doi.org/10.1021/acsami.8b12307.
- Shin, D., Zhu, T., Huang, X., Gunawan, O., Blum, V., and Mitzi, D.B. (2017). Earth-Abundant Chalcogenide Photovoltaic Devices with over 5% Efficiency Based on a Cu₂BaSn(S,Se)₄ Absorber. Adv. Mater. 29, 1606945. https://doi.org/10.1002/adma. 201606945.
- Woo, K., Kim, K., Zhong, Z., Kim, I., Oh, Y., Jeong, S., and Moon, J. (2014). Non-toxic ethanol based particulate inks for low temperature processed Cu₂ZnSn(S,Se)₄ solar cells without S/Se treatment. Sol. Energy Mater. Sol. Cells 128, 362–368. https://doi.org/ 10.1016/j.solmat.2014.06.013.

- Teymur, B., Zhou, Y., Ngaboyamahina, E., Glass, J.T., and Mitzi, D.B. (2018). Solution-Processed Earth-Abundant Cu₂BaSn(S,Se)₄ Solar Absorber Using a Low-Toxicity Solvent. Chem. Mater. 30, 6116–6123. https://doi.org/ 10.1021/acs.chemmater.8b02556.
- Teymur, B., Kim, Y., Huang, J., Sun, K., Hao, X., and Mitzi, D.B. (2022). Top Stack Optimization for Cu₂BaSn(S,Se)₂ Photovoltaic Cell Leads to Improved Device Power Conversion Efficiency beyond 6. Adv. Energy Mater. 12, 2201602. https://doi.org/10.1002/aenm.202201602.
- Bauer, C., Teuscher, J., Brauer, J.C., Punzi, A., Marchioro, A., Ghadiri, E., De Jonghe, J., Wielopolski, M., Banerji, N., and Moser, J.-E. (2011). Dynamics and Mechanisms of Interfacial Photoinduced Electron Transfer Processes of Third Generation Photovoltaics and Photocatalysis. Chimia 65, 704–709. https:// doi.org/10.2533/chimia.2011.704.
- Moser, J.-E. (2010). Dynamics of interfacial and surface electron transfer processes. In Dye-Sensitized Solar Cells (EPFL Press), pp. 403–456. https://doi.org/10.1201/ b16409-16.
- Berera, R., van Grondelle, R., and Kennis, J.T.M. (2009). Ultrafast transient absorption spectroscopy: principles and application to photosynthetic systems. Photosynth. Res. 101, 105–118. https://doi.org/10.1007/s11120-009-9454-y.
- Ghadiri, E., Zakeeruddin, S.M., Hagfeldt, A., Grätzel, M., and Moser, J.-E. (2016). Ultrafast charge separation dynamics in opaque, operational dye-sensitized solar cells revealed by femtosecond diffuse reflectance spectroscopy. Sci. Rep. 6, 24465. https://doi. org/10.1038/srep24465.
- Ghadiri, E., Taghavinia, N., Aghabozorg, H.R., and Iraji zad, A. (2010). TiO₂ nanotubular fibers sensitized with CdS nanoparticles. Eur. Phys. J. Appl. Phys. 50, 20601. https://doi.org/10.1051/ epiap/2010025.
- 15. Ghadiri, E., Taghavinia, N., Zakeeruddin, S.M., Grätzel, M., and Moser, J.-E. (2010). Enhanced

- Electron Collection Efficiency in Dye-Sensitized Solar Cells Based on Nanostructured ${\rm TiO_2}$ Hollow Fibers. Nano Lett. 10, 1632–1638. https://doi.org/10.1021/nl904125q.
- Ghadiri, E., Liu, B., Moser, J.-E., Grätzel, M., and Etgar, L. (2015). Investigation of Interfacial Charge Separation at PbS QDs/(001) TiO₂ Nanosheets Heterojunction Solar Cell. Part. Part. Syst. Char. 32, 483–488. https://doi.org/ 10.1002/ppsc.201400210.
- Ge, J., Koirala, P., Grice, C.R., Roland, P.J., Yu, Y., Tan, X., Ellingson, R.J., Collins, R.W., and Yan, Y. (2017). Oxygenated CdS Buffer Layers Enabling High Open-Circuit Voltages in Earth-Abundant Cu₂BaSnS₄ Thin-Film Solar Cells. Adv. Energy Mater. 7, 1601803. https://doi.org/ 10.1002/aenm.201601803.
- Kessler, R.W., and Wilkinson, F. (1981). Diffuse Reflectance Triplet-Triplet Absorption Spectroscopy of Aromatic Hydrocarbons Chemisorbed on 7-Alumina. J. Chem. Soc., Faraday Trans. 1 77, 309–320. https://doi.org/ 10.1039/F19817700309.
- Wilkinson, F., Willsher, C.J., Uhl, S., Honnen, W., and Oelkrug, D. (1986). Optical detection of a photoinduced thermal transient in titanium dioxide powder by diffuse reflectance laser flash photolysis. J. Photochem. 33, 273–278. https://doi.org/10.1016/0047-2670(86)87089-7.
- Mehl, B.P., Kirschbrown, J.R., House, R.L., and Papanikolas, J.M. (2011). The End Is Different than The Middle: Spatially Dependent Dynamics in ZnO Rods Observed by Femtosecond Pump-Probe Microscopy. J. Phys. Chem. Lett. 2, 1777–1781. https://doi. org/10.1021/j2200809c.
- 21. Van Goethem, E.M., Pinion, C.W., Cating, E.E.M., Cahoon, J.F., and Papanikolas, J.M. (2019). Observation of Phonon Propagation in Germanium Nanowires Using Femtosecond Pump–Probe Microscopy. ACS Photonics 6, 2213–2222. https://doi.org/10.1021/acsphotonics.8b01736.
- 22. Gabriel, M.M., Grumstrup, E.M., Kirschbrown, J.R., Pinion, C.W., Christesen, J.D., Zigler, D.F.,



Cell Reports Physical Science Article

- Cating, E.E.M., Cahoon, J.F., and Papanikolas, J.M. (2014). Imaging Charge Separation and Carrier Recombination in Nanowire p-i-n Junctions Using Ultrafast Microscopy. Nano Lett. 14, 3079–3087. https://doi.org/10.1021/n15012118.
- Zhu, T., Snaider, J.M., Yuan, L., and Huang, L. (2019). Ultrafast Dynamic Microscopy of Carrier and Exciton Transport. Annu. Rev. Phys. Chem. 70, 219–244. https://doi.org/10.1146/annurevphyschem-042018-052605.
- Grumstrup, E.M., Gabriel, M.M., Cating, E.E., Van Goethem, E.M., and Papanikolas, J.M. (2015). Pump-probe microscopy: Visualization and spectroscopy of ultrafast dynamics at the nanoscale. Chem. Phys. 458, 30–40. https://doi. org/10.1016/j.chemphys.2015.07.006.
- Guo, Z., Manser, J.S., Wan, Y., Kamat, P.V., and Huang, L. (2015). Spatial and temporal imaging of long-range charge transport in perovskite thin films by ultrafast microscopy. Nat. Commun. 6, 7471. https://doi.org/10.1038/ ncomms8471.
- Villafana, T.E., Brown, W.P., Delaney, J.K., Palmer, M., Warren, W.S., and Fischer, M.C. (2014). Femtosecond pump-probe microscopy generates virtual cross-sections in historic artwork. Proc. Natl. Acad. Sci. USA 111, 1708– 1713. https://doi.org/10.1073/pnas. 1317230111.
- Robles, F.E., Deb, S., Wilson, J.W., Gainey, C.S., Selim, M.A., Mosca, P.J., Tyler, D.S., Fischer, M.C., and Warren, W.S. (2015). Pumpprobe imaging of pigmented cutaneous melanoma primary lesions gives insight into metastatic potential. Biomed. Opt Express 6, 3631–3645. https://doi.org/10.1364/BOE.6. 003631
- Fukumoto, K., Onda, K., Yamada, Y., Matsuki, T., Mukuta, T., Tanaka, S.i., and Koshihara, S.y. (2014). Femtosecond time-resolved photoemission electron microscopy for spatiotemporal imaging of photogenerated carrier dynamics in semiconductors. Rev. Sci. Instrum. 85, 083705. https://doi.org/10.1063/1. 4893484.
- Teymur, B., Levcenco, S., Hempel, H., Bergmann, E., Márquez, J.A., Choubrac, L., Hill, I.G., Unold, T., and Mitzi, D.B. (2021).
 Optoelectronic and material properties of solution-processed Earth-abundant

- Cu₂BaSn(S, Se)₄ films for solar cell applications. Nano Energy 80, 105556. https://doi.org/10. 1016/j.nanoen.2020.105556.
- Price, M.B., Butkus, J., Jellicoe, T.C., Sadhanala, A., Briane, A., Halpert, J.E., Broch, K., Hodgkiss, J.M., Friend, R.H., and Deschler, F. (2015). Hot-carrier cooling and photoinduced refractive index changes in organic-inorganic lead halide perovskites. Nat. Commun. 6, 8420. https://doi.org/10.1038/ ncomms?420.
- Han, M., Zhang, X., and Zeng, Z. (2017). An investigation of Na-related defects in Cu₂ZnSnSe₄. Phys. Chem. Chem. Phys. 19, 17799–17804. https://doi.org/10.1039/C7CP02192E.
- Liu, B., Guo, J., Hao, R., Wang, L., Gu, K., Sun, S., and Aierken, A. (2020). Effect of Na doping on the performance and the band alignment of CZTS/CdS thin film solar cell. Sol. Energy 201, 219–226. https://doi.org/10.1016/j.solener. 2020.02.088
- Rehan, M., Cho, A., Amare, A.M., Kim, K., Yun, J.H., Cho, J.-S., Park, J.H., Gwak, J., and Shin, D. (2021). Defect passivation in Cu₂ZnSnSe₂ thin-film solar cells by novel sodium doping. Sol. Energy Mater. Sol. Cells 228, 111138. https://doi.org/10.1016/j.solmat.2021.111138.
- Rau, U., and Schmidt, M. (2001). Electronic properties of ZnO/CdS/Cu(In,Ga)Se₂ solar cells

 aspects of heterojunction formation. Thin Solid Films 387, 141–146. https://doi.org/10. 1016/S0040-6090(00)01737-5.
- Choi, W.K., Jung, H.J., and Koh, S.K. (1996). Chemical shifts and optical properties of tin oxide films grown by a reactive ion assisted deposition. J. Vac. Sci. Technol. A 14, 359–366. https://doi.org/10.1116/1.579901.
- Ge, J., and Yan, Y. (2017). Synthesis and characterization of photoelectrochemical and photovoltaic Cu₂BaSnS₄ thin films and solar cells. J. Mater. Chem. C 5, 6406–6419. https:// doi.org/10.1039/C7TC01678F.
- Sardashti, K., Haight, R., Gokmen, T., Wang, W., Chang, L.-Y., Mitzi, D.B., and Kummel, A.C. (2015). Impact of Nanoscale Elemental Distribution in High-Performance Kesterite Solar Cells. Adv. Energy Mater. 5, 1402180. https://doi.org/10.1002/aenm.201402180.

- Bär, M., Schubert, B.-A., Marsen, B., Krause, S., Pookpanratana, S., Unold, T., Weinhardt, L., Heske, C., and Schock, H.-W. (2011). Native oxidation and Cu-poor surface structure of thin film Cu₂ZnSnS₄ solar cell absorbers. Appl. Phys. Lett. 99, 112103. https://doi.org/10.1063/1. 3637574.
- DeMarco, M., Ballard, M., Grage, E., Nourigheimasi, F., Getter, L., Shafiee, A., and Ghadiri, E. (2023). Enhanced photochemical activity and ultrafast photocarrier dynamics in sustainable synthetic melanin nanoparticlebased donor-acceptor inkjet-printed molecular junctions. Nanoscale 15, 14346– 14364. https://doi.org/10.1039/D3NR02387G.
- Kim, Y., Hempel, H., Levcenco, S., Euvrard, J., Bergmann, E., Gunawan, O., Unold, T., Hill, I.G., and Mitzi, D.B. (2021). Optoelectronic property comparison for isostructural Cu₂BaGeSe₄ and Cu₂BaSnS₄ solar absorbers. J. Mater. Chem. A *9*, 23619–23630. https://doi. org/10.1039/D1TA05666B.
- 41. Hong, F., Lin, W., Meng, W., and Yan, Y. (2016). Trigonal Cu₂-II-Sn-VI₄ (II = Ba, Sr and VI = S, Se) quaternary compounds for earth-abundant photovoltaics. Phys. Chem. Chem. Phys. 18, 4828–4834. https://doi.org/10.1039/C5CP06977G.
- Cahen, D., and Noufi, R. (1989). Defect chemical explanation for the effect of air anneal on CdS/CuInSe2 solar cell performance. Appl. Phys. Lett. 54, 558–560. https://doi.org/10. 1063/1.100930.
- Rau, U., Braunger, D., and Schock, H.-W. (1999). Air-Annealing Effects on Polycrystalline Cu(In,Ga)Se₂ Heterojunctions. Solid State Phenom. 67–68, 409–414. https://doi.org/10. 4028/www.scientific.net/SSP.67-68.409.
- Haight, R., Shao, X., Wang, W., and Mitzi, D.B. (2014). Electronic and elemental properties of the Cu₂ZnSn(S,Se)₄ surface and grain boundaries. Appl. Phys. Lett. 104, 033902. https://doi.org/10.1063/1.4862791.
- 45. Teymur, B., Choubrac, L., Hempel, H., Gunawan, O., Unold, T., and Mitzi, D.B. (2022). Influence of Copper Composition on Cu₂BaSn(S,Se)₄ Solution-Deposited Films and Photovoltaic Devices with Over 5% Efficiency. ACS Appl. Energy Mater. 5, 10645–10656. https://doi.org/10.1021/acsaem.2c01364.